PHYSICAL RETRIEVAL OF PRECIPITATION WATER CONTENTS FROM SPECIAL SENSOR MICROWAVE/IMAGER (SSM/I) DATA-PART I: A CLOUD ENSEMBLE/RADIATIVE PARAMETERIZATION FOR SENSOR RESPONSE (report version)

by

William S. Olson and William H. Raymond

Cooperative Institute for Meteorological Satellite Studies

1225 West Dayton Street

University of Wisconsin

Madison, Wisconsin 53706

To be modified and submitted to *J. Appl. Meteor.*

PHYSICAL RETRIEVAL OF PRECIPITATION WATER CONTENTS FROM SPECIAL SENSOR MICROWAVE/IMAGER (SSM/I) DATA- PART I: A CLOUD ENSEMBLE/RADIATIVE PARAMETERIZATION FOR SENSOR RESPONSE (report version)

by

William S. Olson and William H. Raymond

1. INTRODUCTION

The physical retrieval of geophysical parameters based upon remotely sensed data requires a sensor response model which relates the upwelling radiances that the sensor observes to the parameters to be retrieved. In the retrieval of precipitation water contents from satellite passive microwave observations, the sensor response model has two basic components. First, a description of the radiative transfer of microwaves through a precipitating atmosphere must be considered, because it is necessary to establish the physical relationship between precipitation water content and upwelling microwave brightness temperature. Also the spatial response of the satellite microwave sensor (or antenna pattern) must be included in the description of sensor response, since precipitation and the associated brightness temperature field can vary over a typical microwave sensor resolution footprint.

Olson (1989) utilized a simple cuboidal, radiative transfer cloud model to describe the upwelling brightness temperatures at the Scanning Multichannel Microwave Radiometer (SMMR) frequencies. Upwelling brightness temperatures were convolved by approximate radiometer antenna patterns to simulate the antenna temperatures measured by the SMMR. More recently, in applications to aircraft microwave data, Kummerow, et al. (1989) calculated upwelling microwave brightness temperatures for a collection of vertical precipitation profiles, allowing for variations in the total vertically-integrated precipitation by scaling the selected profile. In applications of this method to Special Sensor Microwave/Imager (SSM/I) data, vertically integrated precipitation water contents were assumed to vary lognormally in space within the raining fraction of the radiometer footprint

(Kummerow, 1992). Sensor resolution effects were accomodated by preprocessing the SSM/I data using an antenna pattern matching technique (Robinson, et al., 1992). Xiang, et al. (1992) utilized three-dimensional cloud model simulations as the basis for upwelling brightness temperature calculations at the SSM/I frequencies. The retrieved profiles of cloud and precipitation profiles were those associated with modeled microwave brightness temperatures most consistent with SSM/I observations. An antenna pattern matching technique was utilized to account for the differing spatial resolution of the SSM/I channels; ref. Farrar and Smith (1992).

In the present study, a "population" of convective cells, as well as stratiform clouds, are simulated using a computationally-efficient multi-cylinder cloud model. Ensembles of clouds selected at random from the population, distributed over a 25 km x 25 km model domain, serve as the basis for radiative transfer calculations of upwelling brightness temperatures at the SSM/I frequencies. Sensor spatial response is treated explicitly by convolving the upwelling brightness temperatures by domain-integrated SSM/I antenna patterns. The sensor response model is utilized in precipitation water content retrievals, which is the subject of Part II in this series.

2. DEFINITIONS

The sensor response model describes the physical relationship between the values of geophysical parameters **P** in the earth-atmosphere system, and the antenna temperatures **TA** which the sensor measures. A single antenna temperature measurement TA may respond to variations in several geophysical parameters at different locations; therefore the response model is written $\mathbf{TA(P)}_{mod}$ to represent this multivariate dependency.

It is assumed that the field of geophysical parameters **P** over the sensor swath can be represented by an array of values at discrete grid locations. The gridded domain for SSM/I retrievals is illustrated in Fig. 1. Rectangular grid "boxes" are defined on the grid, such that the center of each box coincides with the earth location of an all-channel antenna

temperature measurement from the SSM/I. The boxes are oriented along the SSM/I A-scans (which contain the all-channel measurements) at a regular spacing of 25 km. Since the cross-scan separation of succeeding A-scan lines varies along the scan line, the cross-scan dimension of the grid boxes also varies, with a maximum dimension of 25 km in the center of the swath, and decreasing towards swath edge. In the discretization of the antenna patterns (Section 3) and brightness temperature fields (Section 4), the variation of the grid box dimension with scan position is taken into account.

In the grid system depicted in Fig. 1, an element of $\mathbf{TA(P)}_{mod}$ is defined by

$$TA(P)_p = A_c{}^T\, TB(P)_p + A_x{}^T\, TB(P)_{p'} + \delta_p\, Tbb, \qquad (1)$$

where A_C and A_X are the co- and cross-polarized antenna patterns of the radiometer, $\mathbf{TB(P)}_p$ and $\mathbf{TB(P)}_{p'}$ are the modeled brightness temperatures in the polarization p and orthogonal polarization p' with respect to the plane of polarization of the measurement, and δ_p is the fraction of the radiometer feedhorn pattern not subtended by the antenna. Tbb is the cosmic background radiance (2.7 K). Each antenna temperature is modeled as the convolution of the upwelling brightness temperature field by the spatial response pattern of the sensor (see section 3 below). In this way, measurements at different channel frequencies or from different sensors which have different sampling / spatial resolution can be accommodated.

In the following sections, the components of the sensor response model, Eq. (1), are described.

3. SENSOR SPATIAL RESPONSE FUNCTIONS

SSM/I measurements are diffraction-limited because the channel wavelengths (1.55 cm to 0.35 cm) are not small in comparison to the antenna dimensions (61 cm x 66 cm); from Hollinger (1991). Aperture diffraction effects cause the breadth of the sensor antenna

patterns to decrease with increasing frequency. The result is a large variation in the effective spatial resolution of the SSM/I.

Measurements of the SSM/I antenna patterns and a detailed description of the SSM/I scan geometry were provided by Poe (1988). Based upon this information, the co- and cross-polarized SSM/I antenna patterns at the earth's surface are calculated for each SSM/I scan position and channel. The patterns are then area-integrated over each grid box in the swath grid and then normalized over all grid boxes to yield spatial response functions. Thus, the sensor spatial response functions $\mathbf{A_C}$ and $\mathbf{A_X}$ give the mean response, for each SSM/I measurement, to brightness temperatures upwelling from each grid box in the swath grid of Fig. 1. Representative normalized spatial response functions at 19.35, 37, and 85.5 GHz are illustrated in Fig. 2. It may be noted from the figure that the sensor spatial response at 19.35 GHz is spread over several grid boxes in the swath grid, indicating relatively low spatial resolution at the grid scale (25 km). In contrast, the spatial response at 85.5 GHz is concentrated almost entirely in a single grid box, indicating high spatial resolution. The spatial response patterns are included in the sensor response model to accomodate the disparity in spatial resolution exhibited by the different channels of SSM/I.

4. CLOUD ENSEMBLE/RADIATIVE MODEL

The relationship between the geophysical parameters **P** and the brightness temperatures $\mathbf{TB_p}$ and $\mathbf{TB_{p'}}$ upwelling from an individual grid box is described using a cloud ensemble/radiative model. The model geometry is illustrated in Fig. 3. The horizontal dimensions of the domain are 25 km x 25 km, the nominal grid box dimension, with a vertical dimension of 20 km. Typically, within a region of these dimensions, an array of convective clouds as well as anvil-type or stratiform cloud may coexist. Both types of cloud are simulated in this study, with a brief summary given below.

4.1 Model Description

Individual cloud simulations are performed using two versions of the multi-cylinder cloud model of Ridout (1991, 1993). Ridout's original model (ref. 1991, 1993) is utilized for convective cloud simulations. It is a time-dependent, non-hydrostatic cloud model which utilizes six concentric, quasi-cylindrical regions to represent the horizontal exchange of heat and moisture between the core region of the modeled convective cell and its immediate environment. The vertical momentum equation is represented explicity only in the innermost cylinder (core) of the cloud model, thereby reducing computational requirements substantially. The model includes a parameterization for the effects of vertical wind shear on the entrainment/detrainment of liquid water and other cloud variables.

The treatment of microphysics follows the development by Lin, et al. (1983), with some modifications by Ferrier (1988). The model predicts the distributions of cloud water and cloud ice, rain, snow, and graupel/hail at levels separated by 300 m in the vertical, averaged over each cylindrical region.

A model cloud is initially forced by a prescribed sub-cloud vertical velocity distribution over a prescribed period (900 s in the current study), after which time the forcing is removed and the cloud continues to develop according to model dynamics. This method of initiation is used to simulate gust-front forcing of convective clouds. Cloud development is also controlled by a prescribed minimum updraft radius which is the radial dimension of the updraft (third cylinder) at midlevels in the troposphere. The radii of the other cylinders are all scaled according to the prescribed updraft radius.

A second version of the Ridout (1992) model is developed to simulate stratiform anvil-type precipitation distributions in this study. In this version of the model, the five surrounding cylinders are eliminated, and it is assumed that the distributions of all cloud variables both inside and outside the remaining cylinder are identical. In other words, a strictly one-dimensional simulation is performed. In addition, the vertical velocity distribution is prescribed to be a double-parabolic profile, with a downdraft below the

freezing level and an updraft aloft. This type of vertical velocity profile is generally consistent with observations documented by Leery and Houze (1979), Gamache and Houze (1982), Marks and Houze (1987), and Rutledge and Houze (1987), who observed mesoscale updrafts and downdrafts in several tropical and midlatitude storms. The Lin/Ferrier cloud microphysical parameters are altered to reflect the variability of particle size distributions noted by Houze, et al. (1979) and Stewart, et al. (1984). Stratiform cloud simulations are performed by integrating the model forward in time until equilibrium distributions of all cloud variables are obtained, usually after 10 hours of simulation time.

4.2 Cloud Environment

The cloud environment for both convective and stratiform cloud simulations is taken from the GATE Day 261 rawinsonde profile; ref. Ferrier and Houze (1989). Profiles of pressure, temperature, water vapor mixing ratio, and horizontal wind components are interpolated to levels at 150 m altitude spacing in the Ridout model.

4.3 Generation of Ensembles - Convective Clouds

By varying the minimum updraft radius and the basal updraft vertical velocity in the Ridout model, a variety of clouds ranging from shallow to deep convection are simulated. Combinations of eight cloud radii between 0.5 and 5 km and four basal updrafts between 2 and 8 m/s are used to generate 32 different cloud simulations. For each cloud simulation an effective cloud lifetime is computed. For the purpose of this study the lifetime of a simulated cloud is defined as the period over which the average reflectivity of the cloud core volume (a cylindrical region 2.43 km in radius and 9.49 km in height) exceeds 30 dBZ. Effectively, these are the cloud radar echo lifetime criteria that were used by López (1977) in his study of tropical clouds. The core volume dimensions are designed to simulate the radar volume of the airborne APS-20 radar utilized in López' study.

Based upon the radar echo lifetime statistics compiled by López (1977), a "population" of simulated clouds is created. In López' study, tropical clouds were found to have echo lifetimes that were lognormally distributed. A plot of this observed lifetime

distribution is reproduced in Fig. 4. A simulated cloud with a given lifetime is assumed to occur with the same relative frequency as a cloud with the same observed lifetime in López' radar study.

A random number generator is utilized to select simulated clouds from the population and create an ensemble within the 25 km x 25 km model domain (see Fig. 3). Once a cloud is selected from the population, a cloud lifestage is also randomly selected. The cloud from that stage of the simulation is then positioned at random within the model domain. Another cloud is then selected at random from the assumed population, and the procedure is repeated. The only restriction on cloud placement is that the updrafts of no two simulated clouds may overlap. By varying the number of clouds selected for the ensemble, a wide range of cloud configurations with different water and ice contents can be simulated. In this study, 350 different cloud ensembles containing between 8 and 56 clouds are created using the procedure outlined above. One such ensemble based upon 48 simulated clouds is depicted in Fig. 5. In the figure, image intensity is proportional to the slant-path integrated water contents at the SSM/I viewing incidence angle (53.1 degrees from zenith).

4.4 Generation of Ensembles - Stratiform Clouds

Different stratiform clouds are generated by varying the amplitude of the prescribed updraft and downdraft distributions. Following the diagnostics studies of Gamache and Houze (1982), in which the magnitudes of updraft and downdraft velocities were estimated for tropical anvils, a range of representative updraft and downdraft amplitudes are selected. Updraft amplitudes are varied from 0.05 to 0.50 m/s, while downdraft amplitudes are varied from 0.00 to -0.50 m/s, to create a total of 42 stratiform simulations.

4.5 Radiance Calculations

Both convective and stratiform cloud ensembles are located within the model domain depicted in Fig. 3. The 25 km x 25 km x 20 km model domain is subdivided into a grid with a horizontal grid spacing of 0.500 km, and a vertical grid spacing of 0.375 km.

Pressure, temperature, water vapor density, and the equivalent water contents of precipitating and non-precipitating particles from the simulated clouds are interpolated to grid locations within the domain. In addition, cloud latent heating rates are evaluated at grid locations. The average surface rainfall rate over the domain is also computed.

The cloud and environmental parameters at each grid location are used to calculate the associated microwave radiative properties (i.e., the extinction coefficients, single-scatter albedoes, and asymmetry factors). Molecular oxygen and water vapor extinction coefficients are computed using the Liebe (1985) model. Microwave radiative parameters for precipitating liquid and ice hydrometeors are computed using the formulae of Kummerow and Weinman (1988). Rayleigh theory is employed to calculate the extinction coefficients of nonprecipitating cloud particles. At the base of the grid a surface skin temperature and microwave emissivities characteristic of both land and ocean surfaces are assigned. The downwelling cosmic background brightness temperature (2.7 K) is specified at the top of the model domain.

A forward radiative transfer calculation is performed to determine the distribution of microwave brightness temperatures upwelling from each cloud ensemble domain. A radiative transfer solution based upon Eddington's second approximation is utilized to accomodate the multiple scattering effects of precipitating hydrometeors at microwave frequencies. Brightness temperatures are computed at the SSM/I frequencies (19.35, 22.235, 37, and 85.5 GHz) in both vertical and horizontal polarizations at an incidence angle of 53.1 degrees. Since radiance paths at oblique incidence can exit the sides of the model domain, it is assumed that the domain, and all cloud and environmental properties, are periodic in the horizontal.

Fields of brightness temperatures upwelling from the convective cloud ensemble of Fig. 5 are depicted in Fig. 6 (over a low-emissivity background characteristic of the ocean), and in Fig. 7 (over a high-emissivity backgound characteristic of a land surface). Comparing the figures, it may be noted that the ocean background provides a good

radiative contrast to regions of greater emission from liquid precipitation, while the higher-emissivity land background provides less contrast. Over either background, the low brightness temperatures at 85.5 GHz associated with scattering by precipitating ice particles are evident. The basic differences between liquid and ice precipitation signatures provide the motivation for the radiative parameterization described in the next section.

Ensemble-average, horizontally-polarized brightness temperatures are plotted against the corresponding ensemble-average slant path-integrated precipitating liquid water contents for the four SSM/I frequencies in Fig. 8. The brightness temperature calculations in these plots utilize an emissivity of 0.3, characteristic of an ocean surface. Both convective and stratiform ensemble calculations are included in the figure. Plotted numbers in the figure are the ensemble-average slant-path integrated ice water contents, thresholded at integral values.

It may be noted from the figure that there is a significant spread of brightness temperatures corresponding to a given liquid precipitation path, due to variations in ice water content, precipitation area, non-precipitating cloud amount, and cloud geometry. The scattering effect of ice precipitation is most obvious at 37 and 85.5 GHz, leading to somewhat lower brightness temperatures for a given precipitating liquid path. At 85.5 GHz, the stratiform ensembles yield brightness temperatures which are significantly lower than the convective ensemble brightness temperatures, due to the relatively high amounts of precipitating ice (relative to precipitating liquid) in the stratiform clouds. The focus of the next section will be to parameterize the ensemble-average upwelling brightness temperatures as functions of the precipitating liquid and ice paths.

5. RADIATIVE PARAMETERIZATION OF CLOUD ENSEMBLE/ RADIATIVE CALCULATIONS

The cloud ensemble/radiative calculations provide a fairly detailed and accurate description of the upwelling brightness temperature field for a given cloud ensemble configuration. However, the sensor response model (Eq. 1) requires a functional

relationship between the grid box average brightness temperatures ($\mathbf{TB_p}$ and $\mathbf{TB_{p'}}$) and properties of the cloud field and its environment (geophysical parameters **P**). This functional relationship, or parameterization, must include a meaningful description of the precipitation field and produce an accurate representation of the detailed cloud ensemble/radiative calculations. However, since the sensor response model will ultimately be utilized in retrievals, the number of geophyical parameters **P** must be consistent with the sampling of the SSM/I. The SSM/I provides only 13 brightness temperture measurements per grid box in the swath grid of Fig. 1., and it is likely that some of the information in these measurements is redundant. Thus the number of parameters must be kept small in order to avoid ambiguous retrievals; i.e. the number of unknown parameters **P** in the retrieval must be less than the number of independent measurements. Our strategy is to select parameters which describe the mean cloud and environmental characteristics of each grid box, and then parameterize smaller scale variability.

Figures 5 through 7 illustrate the basic relationships between precipitating liquid and ice contents and upwelling microwave brightness temperatures. There is a strong correlation between the path-integrated precipitating water content and the upwelling brightness temperature at 37 GHz. The same correlation is observed in the 19.35 and 22.235 GHz simulations (not shown). At 85.5 GHz, the path-integrated precipitating ice content is strongly anticorrelated with upwelling brightness temperature.

These relationships suggest a simple parameterization for the average upwelling brightness temperature from a given swath grid box. The full three-dimensional radiative calculation is replaced by four one-dimensional calculations. The first calculation is performed for the brightness temperature upwelling from the cloud-free environment of the grid box. The second assumes that only precipitating liquid is present in the model atmosphere; the third only precipitating ice, and the fourth for a model atmosphere containing both precipitating liquid and ice. Vertical profiles of precipitating liquid and ice in the one-dimensional radiative calculations are represented by analytical curve fits to the

horizontally-averaged profiles of both the convective and stratiform cloud ensembles. Both precipitating liquid and ice equivalent water contents are given by

$$\mathrm{PLWC} = \begin{cases} 0, & z > \mathrm{zmax} \\ A \cdot \sin\left(\pi\,(z - \mathrm{zmin})/(\mathrm{zmax} - \mathrm{zmin})\right) & \\ \quad \cdot \exp\left(-\{B1 + B2/\mathrm{PLWP}\} \cdot (z - \mathrm{zmin})/(\mathrm{zmax} - \mathrm{zmin})\right), & \\ \qquad \mathrm{zmin} < z < \mathrm{zmax} & \\ 0, & z < 0 \end{cases} \tag{2}$$

Here, PLWC is the precipitating liquid or ice equivalent water content, PLWP is the slant path-integrated precipitating liquid or ice depth, zmin and zmax are the lower and upper altitude bounds of the water content profile, and B1 and B2 are fitting constants. Given the slant path-integrated precipitating liquid water or ice depth, the constant A is set such that the integrated analytical profile yields the same depth. The constants zmin, zmax, B1, and B2 are all optimized to yield the minimum mean-square difference between the water content profiles generated by the cloud ensembles and those calculated using Eq. (2). Values of the adjustable parameters and statistics of the analytical profile approximation are listed in Table 1.

The mean profiles and analytical curve fits for convective liquid and ice precipitation are shown in Figs. 9 and 10, respectively. Similar curve fits are obtained for the stratiform cloud ensembles. The mean error standard deviation in the estimated water contents from the analytical profiles is about 0.03 g/m^3.

The four one-dimensional calculations are combined in proportion to the fractional coverage of liquid and ice precipitation that are observed along the oblique viewing angle of the SSM/I. Although it is assumed that precipitating liquid and ice occupy specified fractions, no assumption is made concerning the relative positions of the liquid and ice

fractions with respect to one another inside the grid box. If f_l and f_i are the fractions of precipitating liquid and ice, respectively, then the parameterized upwelling brightness temperature at a given frequency and polarization is given by

$$TB(P) = (1 - f_l)(1 - f_i)\,TB_c + f_l(1 - f_i)\,TB_l + (1 - f_l)\,f_i\,TB_i + f_l\,f_i\,TB_{li}\,. \quad (3)$$

Here, TB_c, TB_l, TB_i, and TB_{li} are the brightness temperatures upwelling from a cloud-free model atmosphere, an atmosphere containing only precipitating liquid, an atmosphere containing only preciptating ice, and an atmosphere containing both precipitating liquid and ice, respectively.

Although Eq. (3) is a fairly good approximation to the brightness temperatures upwelling from the stratiform cloud ensembles, the small-scale variability of precipitation water paths in the convective ensembles leads to discrepancies which cannot be parameterized so easily. To account for the variability of water paths, the presence of nonprecipitating clouds, and other factors, the liquid and ice precipitation water contents in the analytical profiles are adjusted to obtain better agreement with the detailed brightness temperature calculations. This strategy follows the modeling efforts of Short and North (1990), and Hinton, et al. (1992), who noted that the brightness temperature response to the average precipitation rate is less if the rain rates are gamma or lognormally distributed, rather than uniformly distributed. Thus, the effective liquid and ice precipitation water contents are expressed as power-law functions of the original water contents (from the analytical profiles), to accomodate the difference in response.

$$PLWC' = \alpha\ PLWC^{\beta} \quad (4)$$

Here PLWC is the original liquid or ice water content. The power-law constants α and β are adjusted to minimize the difference between the parameterized brightness temperatures, Eq. (3), and those computed from the cloud ensemble/radiative calculations. Separate power-law constants are computed for the convective and stratiform ensembles. Best-fit power law constants and parameterization errors are summarized in Table 2. Also scatterplots of the parameterized brightness temperatures vs. the cloud ensemble brightness temperatures at the four SSM/I frequencies are presented in Fig. 11.

It may be noted from Table 2 that the power-law constants used to modify the convective precipitating liquid water contents at 19.35, 22.235, and 37 GHz are all significantly less than 1, indicating a substantial reduction in the effective water content utilized in the radiative parameterization. This result is consistent with the study of Hinton, et al. (1992), who noted a reduced response of upwelling brightness temperature to mean rainfall rate if the rainfall rates within a given region are gamma-distributed. The power-law constants used to modify the stratiform precipitating liquid water contents are closer to 1, which is reasonable since the parameterization appoximates the precipitation field by a horizontally-uniform field, and the stratiform cloud ensembles have horizontally-uniform structure.

The power-law constants for convective ice precipitation defy a simple physical interpretation; however, the power-law constants used to modify the stratiform precipitating ice equivalent water contents are close to 1. Again, the horizontally-uniform clouds in the radiative parameterization are a good approximation to the true structure of the stratiform cloud ensembles, so only a slight modification of the water contents is required.

The statistics in Table 2 and the scatterplots in Fig. 11 indicate parameterization errors which are typically small, but which increase with increasing frequency. It should be noted that the absolute accuracy of SSM/I antenna temperature measurements is on the order of $\pm$ 3 K (Hollinger, 1991). The most serious parameterization errors are attributed to the strongly convective ensembles which produce brightness temperatures between 180 K and

200 K at 85.5 GHz (see Fig. 11d). Scattering by precipitation-sized ice particles is strongest for these convective clouds at 85.5 GHz, and the horizontally-homogeneous cloud approximation utilized in the parameterization is least suitable under these conditions.

In the retrieval scenario it will not be known *a priori* whether a given brightness temperature is upwelling from a convective or stratiform cloud field. Therefore, a simple discriminant based upon the relative proportions of liquid and ice precipitation is devised. The distribution of ice vesus liquid preciptation paths of the convective and stratiform ensembles is shown in Figure 12. It may be noted that the ratio of ice to liquid paths is much smaller in the convective ensembles than in the stratiform ensembles. In the convective ensembles, the ratio of ice precipitation path to the total path, designated r_{ice}, is always less than 0.5, while in the stratiform ensembles it typically exceeds 0.8. In this study it is assumed that if r_{ice} is less than 0.5, the convective parameterization for brightness temperature is used. If r_{ice} is greater than 0.8, then the stratiform parameterization is employed. For ratios between 0.5 and 0.8, it is assumed that the precipitation water paths have both convective and stratiform components, the proportion of each being determined by linear interpolation.

6. CONCLUDING REMARKS

The cloud ensemble/radiative parameterization described herein provides a computationally-efficient means of simulating microwave antenna temperatures at the SSM/I frequencies. The parameterization is therefore useful in physical retrieval applications where many thousands of antenna temperature computations must be performed over a single solution domain (see Part II of this series). The partitioning of cloud fields into separate convective and stratiform components is an obvious simplification, since generally speaking there are dynamical and thermodynamic interactions between the convective and stratiform regions of an organized precipitating storm; ref. Rutledge and Houze (1987). The cloud ensemble/radiative parameterization

could be generalized by simulating cloud fields in a fully 3-dimensional cloud model and parameterizing the bulk precipitation structure and radiance fields as in the current study.

Other data from the SSM/T, SSM/T-2, and infrared sensors could be included in physical retrievals by specifying the appropriate sensor spatial response characterisitics and channel frequencies in the cloud ensemble/radiative parameterization. The addition of these sensor data will be the subject of future study.

Acknowledgments

The authors wish to thank Robert Aune, Scott Braun, George Diak, Brad Ferrier, Barry Hinton, James Hollinger, Robert Houze, Jr., Christian Kummerow, Lynn McMurdie, Gene Poe, Robert Rabin, James Ridout, David Short, Bill Smith, Matthias Steiner, James Weinman, Mark Whipple and Harold Woolf for their help and inspiration during various phases of this study. This work was supported by NASA Grant NAGW-1855. One author (WHR) was supported in part by National Science Foundation Grant ATM-8920508.

REFERENCES

Farrar, M.R., and E.A. Smith, 1992: Spatial resolution enhancement of terrestrial features using deconvolved SSM/I microwave brightness temperatures. IEEE Trans. Geosci. Remote Sens., 30, 349-355.

Ferrier, B.S., 1988: One-dimensional time-dependent modeling of squall-line convection. Ph.D. thesis, University of Washington, Seattle, Washington, 259 pp.

Ferrier, B.S., and R.A. Houze, Jr., 1989: One-dimensional time-dependent modeling of deep convection. Part I: Model dynamics and simulations of GATE cumulonimbus clouds. J. Atmos. Sci., 46, 330-352.

Gamache, J.F., and R.A. Houze, Jr., 1982: Mesoscale air motions associated with a tropical squall line. Mon. Wea. Rev., 110, 118-135.

Hinton, B.B., W.S. Olson, D.W. Martin, and B. Auvine, 1992: A passive microwave algorithm for tropical oceanic rainfall. J. Appl. Meteor., 31, 1379-1395.

Hollinger, J.P. (ed.), 1991: DMSP Special Sensor Microwave/Imager Calibration/Validation Final Report Volume I. Naval Research Laboratory, Washington, D.C.

Houze, R.A., Jr., P.V. Hobbs, P.H. Herzegh, and D.B. Parsons, 1979: Size distributions of precipitation particles in frontal clouds. J. Atmos. Sci., 36, 156-162.

Kummerow, C.D., and J.A. Weinman, 1988: Radiative properties of deformed hydrometeors at commonly used passive microwave frequencies. IEEE Trans. Geosci. Remote Sens., 26, 629-638.

Kummerow, C., R.A. Mack, and I.M.Hakkarinen, 1989: A self-consistency approach to improve microwave rainfall rate estimation from space. J. Appl. Meteor., 28, 869-884.

Kummerow, C., 1992: personal communication. Currently with Goddard Space Flight Center, Greenbelt, Maryland.

Leery, C.A., and R.A. Houze, Jr., 1979: Melting and evaporation of hydrometeors in precipitation from the anvil clouds of deep tropical convection. J. Atmos. Sci., 36, 669-679.

Liebe, H.J., 1985: An updated model for millimeter wave propagation in moist air. Radio Science, 20, 1069-1089.

López, R.E., 1977: The lognormal distribution and cumulus cloud populations. Mon. Wea. Rev., 105, 865-872.

Lorenc, A.C., 1986: Analysis methods for numerical weather prediction. Quart. J. R. Met. Soc., 112, 1177-1194.

Lin, Y.-L., R.D. Farley, and H.D. Orville, 1983: Bulk parameterization of the snow field in a cloud model. J. Climate Appl. Meteor., 22, 1065-1092.

Marks, F.D., and R.A. Houze, Jr., 1987: Inner core structure of Hurricane Alicia from airborne doppler radar observations. J. Atmos. Sci., 44, 1296-1317.

Olson, W.S., 1989: Physical retrieval of rainfall rates over the ocean by multispectral microwave radiometry- application to tropical cyclones. J. Geophys. Res. - Atmospheres, 94, 2267 - 2280.

Poe, G., 1988: personal communication. Currently with Aerojet Electronics Systems Division, Azusa, California.

Ridout, J.A., 1991: A Parameterized Quasi-Five-Cylinder Convective Cloud Model and Its Application to Remote Sensing of Rainfall. Ph.D. thesis, University of Wisconsin, Madison, Wisconsin, 278 pp.

Ridout, J.A., 1992: personal communication. Currently with Naval Research Laboratory-West, Monterey, California.

Ridout, J. A., 1993: A quasi-five-cylinder model of deep convection. Part I: Updraft growth in non-sheared environments. Submitted to J. Atmos. Sci..

Robinson, W.D., C. Kummerow, and W.S. Olson, 1992: A technique for matching and enhancing the resolution of microwave measurements from the SSM/I instrument. IEEE Trans. Geosci. Remote Sens., 30, 419-429.

Rutledge, S.A., and R.A. Houze, 1987: A diagnostic modeling study of the trailing stratiform region of a midlatitude squall line. J. Atmos. Sci., 44, 2640-2656.

Short, D.A., and G.R. North, 1990: The beam filling error in the Nimbus 5 Electronically Scanning Microwave Radiometer observations of Global Atlantic Tropical Experiment rainfall. J. Geophys. Res., 95, 2187-2193.

Simpson, J., R.F. Adler, G.R. North, 1988: A proposed Tropical Rainfall Measuring Mission (TRMM) Satellite. Bull. Amer. Met. Soc., 69, 278-295.

Stewart, R.E., J.D. Marwitz, J.C. Pace, and R.E. Carbone, 1984: Characteristics through the melting layer of stratiform clouds. J. Atmos.Sci., 41, 3227-3237.

Xiang, X., E.A. Smith, and G.J. Tripoli, 1992: A cloud and radiation model-based algorithm for rainfall retrieval from SSM/I multispectral microwave measurements. Proceedings of the Sixth Conference on Satellite Meteorology and Oceanography, Atlanta, Georgia, 286-289.

Table 1. Parameters of the best-fit analytical precipitating water content profiles, based upon the convective and stratiform cloud ensemble simulations. Adjustable parameters zmin and zmax are in units of kilometers, B1 is dimensionless, and B2 has units of m^2/kg. Parameters associated with the liquid and ice precipitation profiles are listed separately. The analytical convective profiles have a combined bias of -2.6×10^{-5} g/m^3, and an error standard deviation of 0.037 g/m^3. The analytical stratiform profiles have a combined bias of 1.1×10^{-4} g/m^3, and and error standard deviation of 0.028 g/m^3.

	zmin	zmax	B1	B2
Convective liquid:	-0.84	6.19	1.81	1.67
Convective ice:	3.75	15.20	5.25	3.22
Stratiform liquid:	-0.77	5.07	0.99	-0.29
Stratiform ice:	3.13	10.70	3.21	-0.37

Table 2. Best-fit power-law constants in the cloud ensemble/radiative parameterization at the SSM/I frequencies. Constants are listed separately for convective and stratiform cloud ensembles. Also listed are the bias and error standard deviation of the parameterized brightness temperatures with respect to the brightness temperatures generated from the cloud ensembles.

	α_{liq}	β_{liq}	α_{ice}	β_{ice}
19.35 GHz				
convective:	.350	.400	1.428	.857
stratiform:	.937	.953	.930	.855
bias = -.138 K				
σ_{err} = 1.693 K				
22.235 GHz				
convective:	.327	.393	1.284	.950
stratiform:	.795	.874	.920	.857
bias = -.208 K				
σ_{err} = 1.036 K				
37 GHz				
convective:	.244	.356	.820	.864
stratiform:	.916	.959	.982	.924
bias = -.766 K				
σ_{err} = 2.430 K				
85.5 GHz				
convective:	.883	1.464	.187	.417
stratiform:	.988	1.023	1.021	.982
bias = -.538 K				
σ_{err} = 3.165 K				

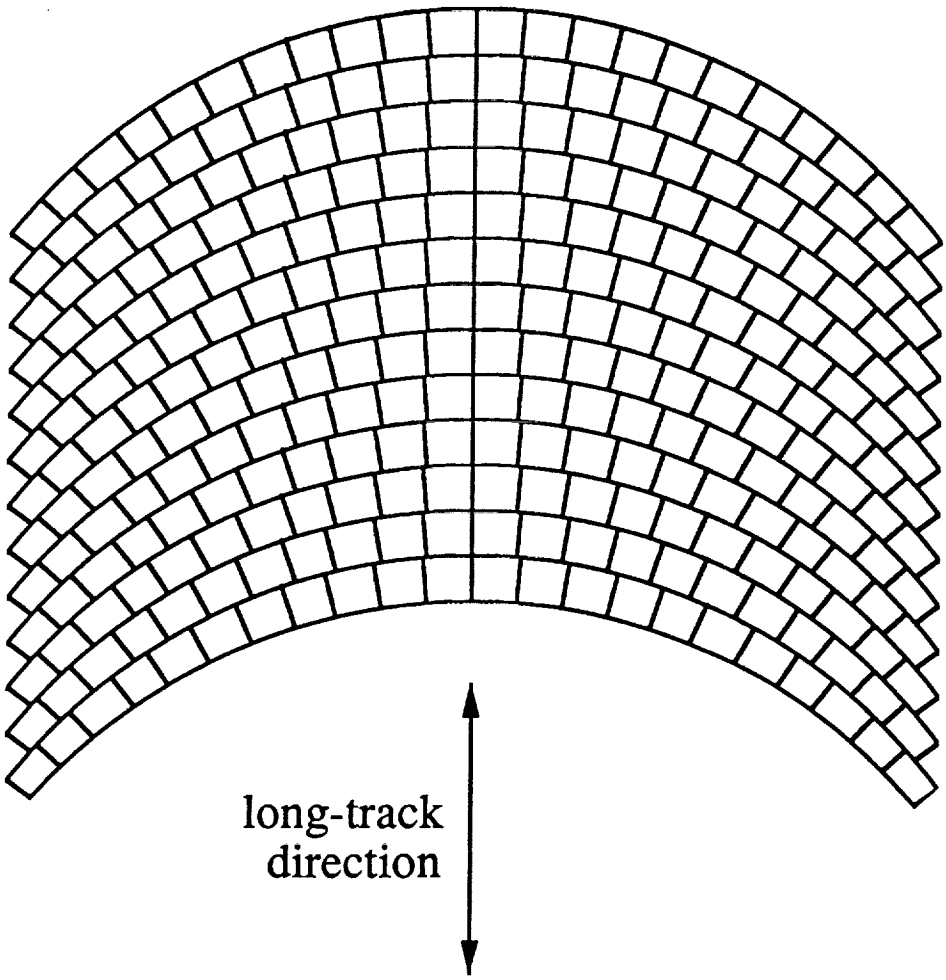

Fig. 1. Schematic of the SSM/I swath grid. For clarity, grid box sizes have been magnified by a factor of three.

(a) 19.35 GHz normalized response

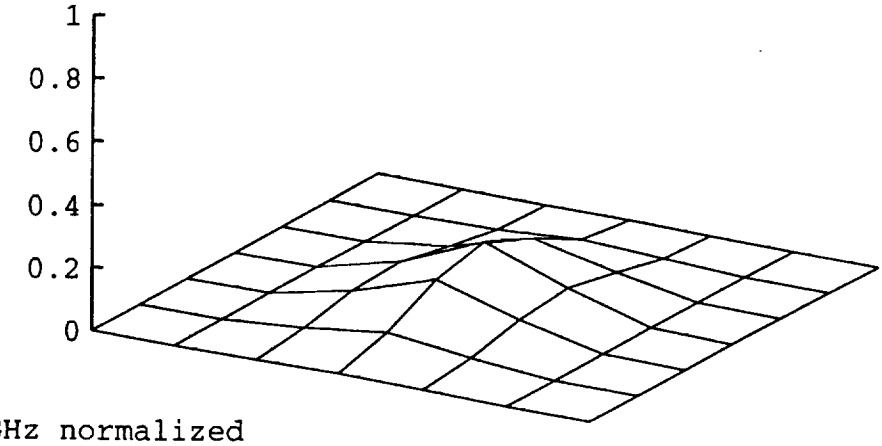

(b) 37 GHz normalized response

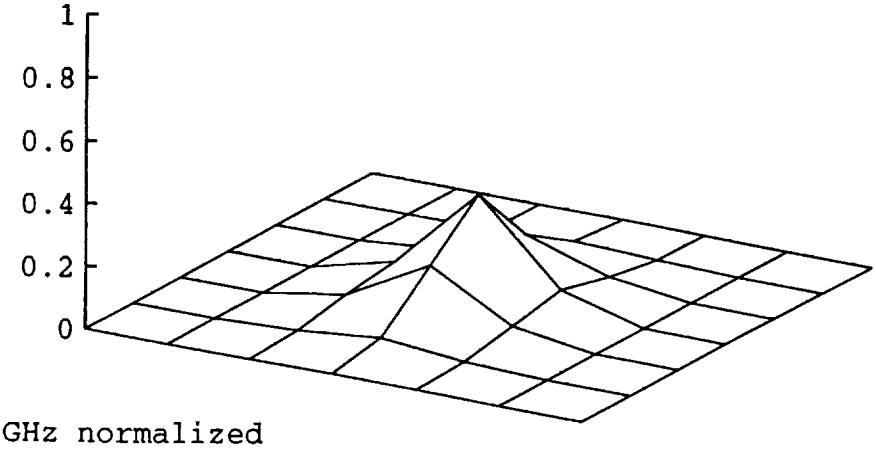

(c) 85.5 GHz normalized response

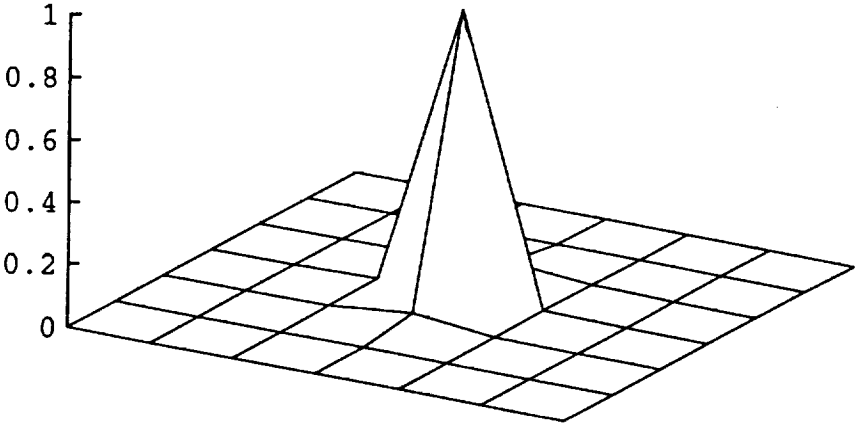

Fig. 2. Co-polarized SSM/I response functions at (a) 19.35 GHz, (b) 37 GHz, and (c) 85.5 GHz in the vertical polarization channels.

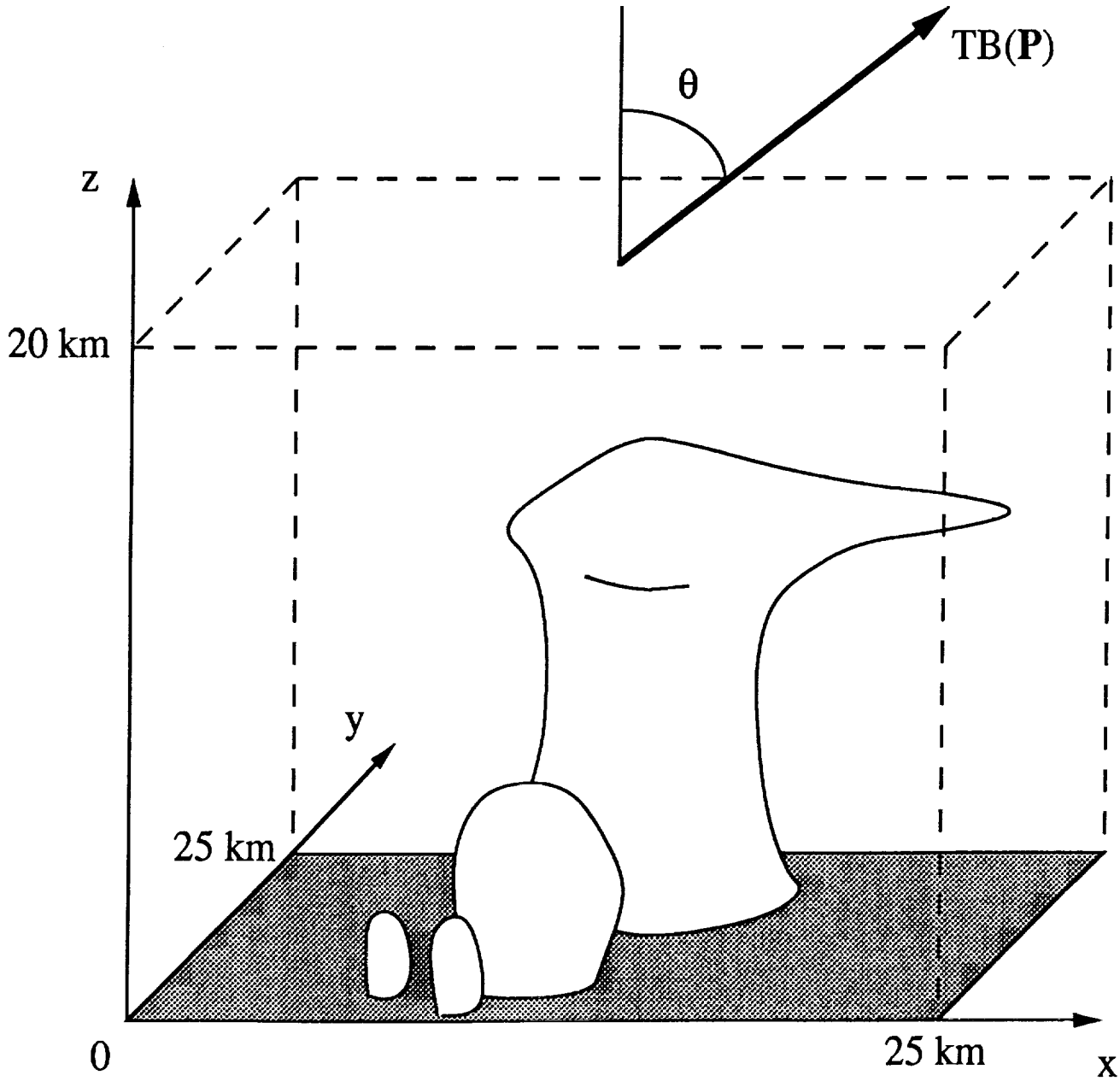

Fig. 3 Domain of the cloud ensemble/radiative model. Model dimensions are 25 km x 25 km x 20 km. Upwelling brightness temperatures are computed along an oblique path at angle $\theta = 53.1$ from zenith.

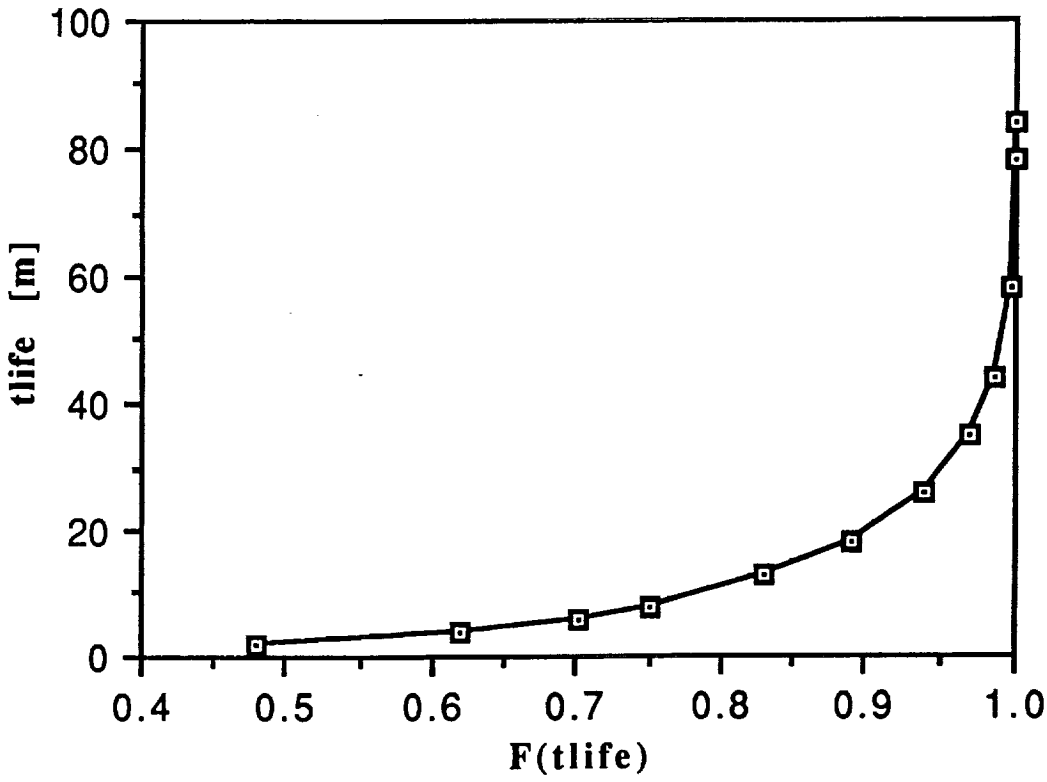

Fig. 4. Radar echo lifetime cumulative distribution from López (1977). The cloud radar echo lifetime tlife, in minutes, is plotted against the cumulative fraction of clouds F with lifetimes less than tlife.

(a)

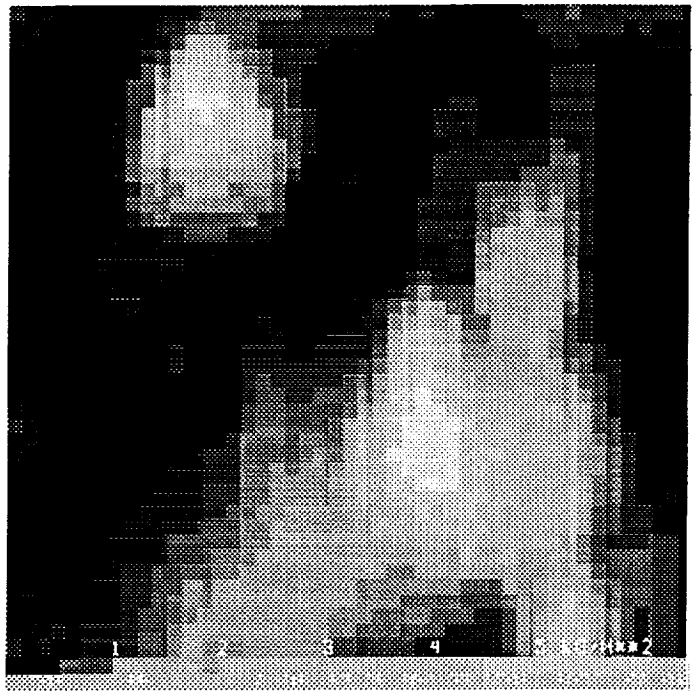

(b)

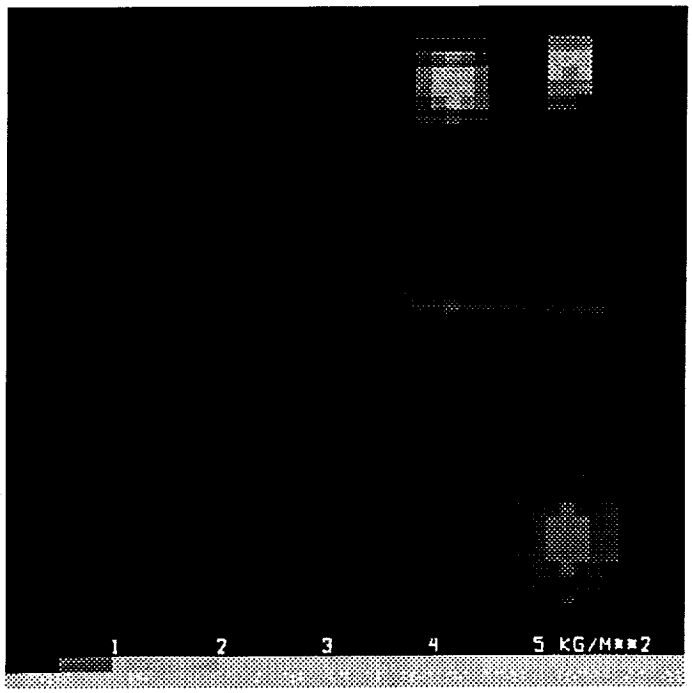

Fig. 5. Imagery of (a) path integrated precipitating liquid water and (b) path integrated precipitating ice from the cloud ensemble/radiative model. The precipitation path distributions are generated from an ensemble of 48 convective cloud simulations. The area represented by each panel is 25 km x 25 km.

(a)

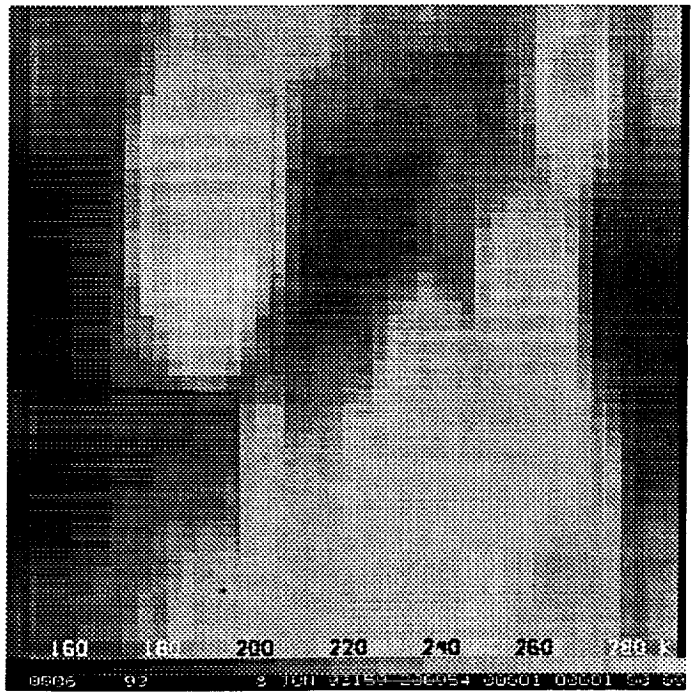

(b)

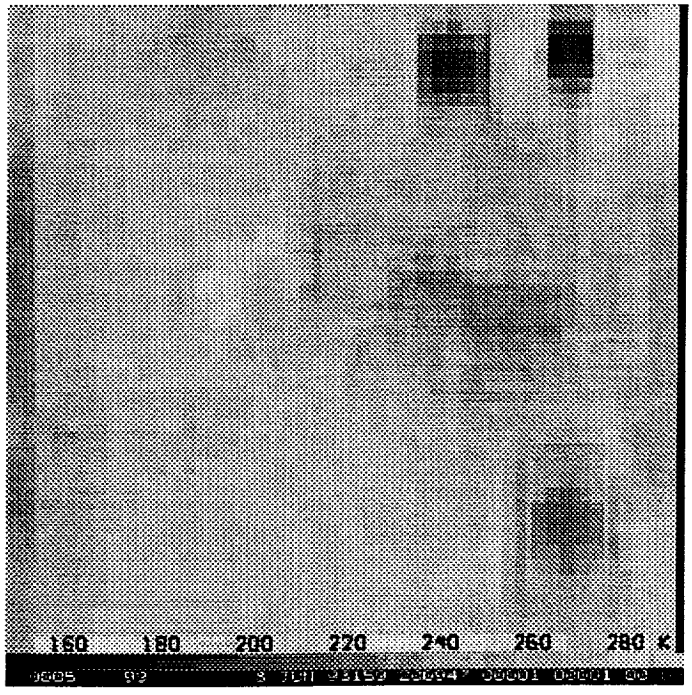

Fig. 6. Computed brightness temperature field at (a) 37 GHz, and (b) 85.5 GHz, upwelling from the convective cloud ensemble shown in Fig. 5. A surface emissivity of 0.30 is assumed. The area represented by each panel is approximately 25 km x 25 km.

(a)

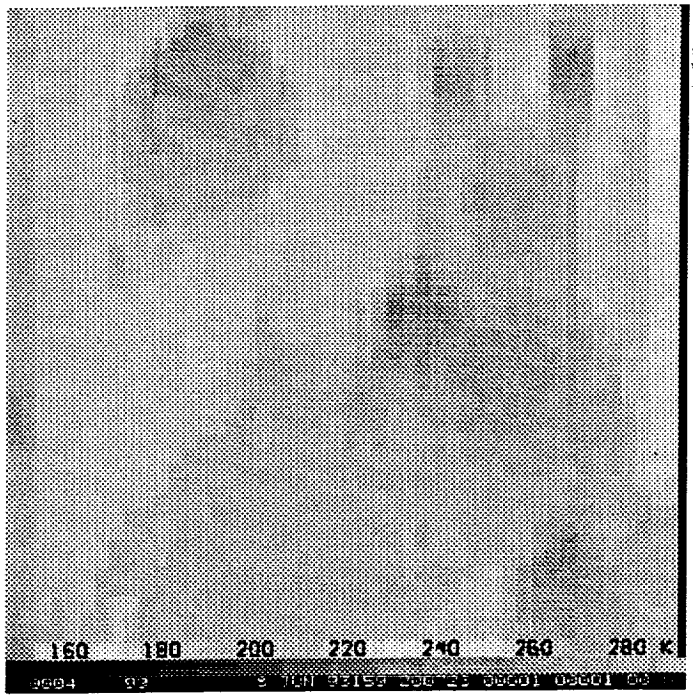

(b)

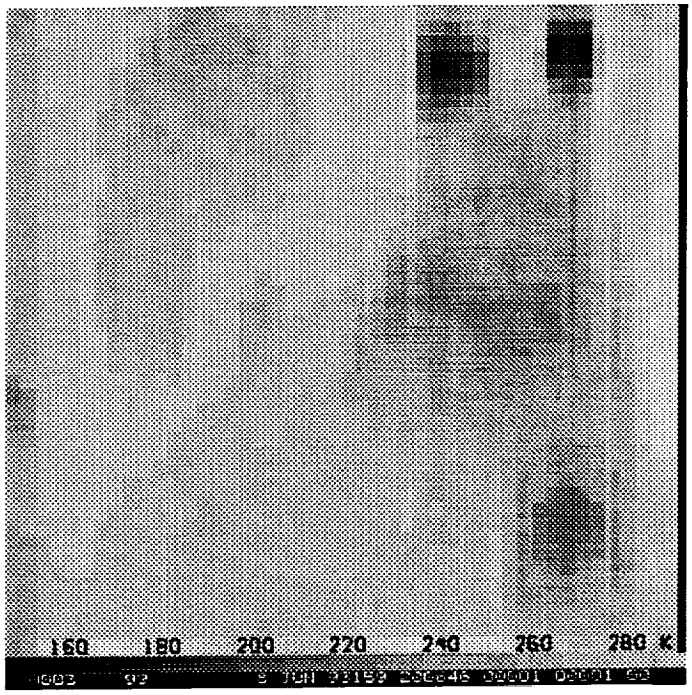

Fig. 7. Computed brightness temperature field at (a) 37 GHz, and (b) 85.5 GHz, upwelling from the convective cloud ensemble shown in Fig. 5. A surface emissivity of 0.95 is assumed. The area represented by each panel is approximately 25 km x 25 km.

(a)

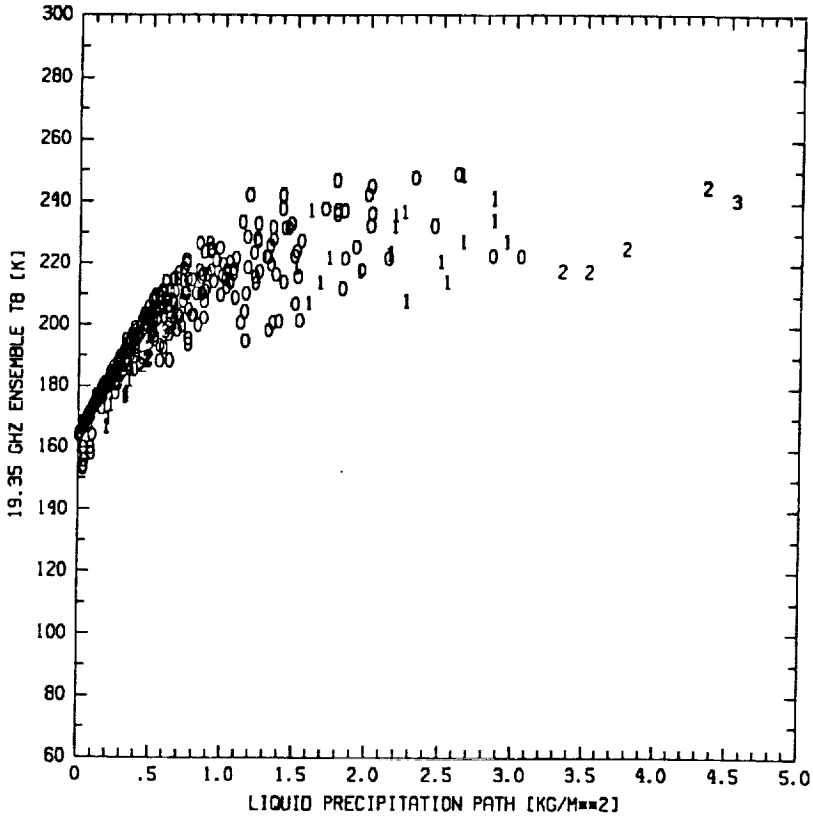

(b)

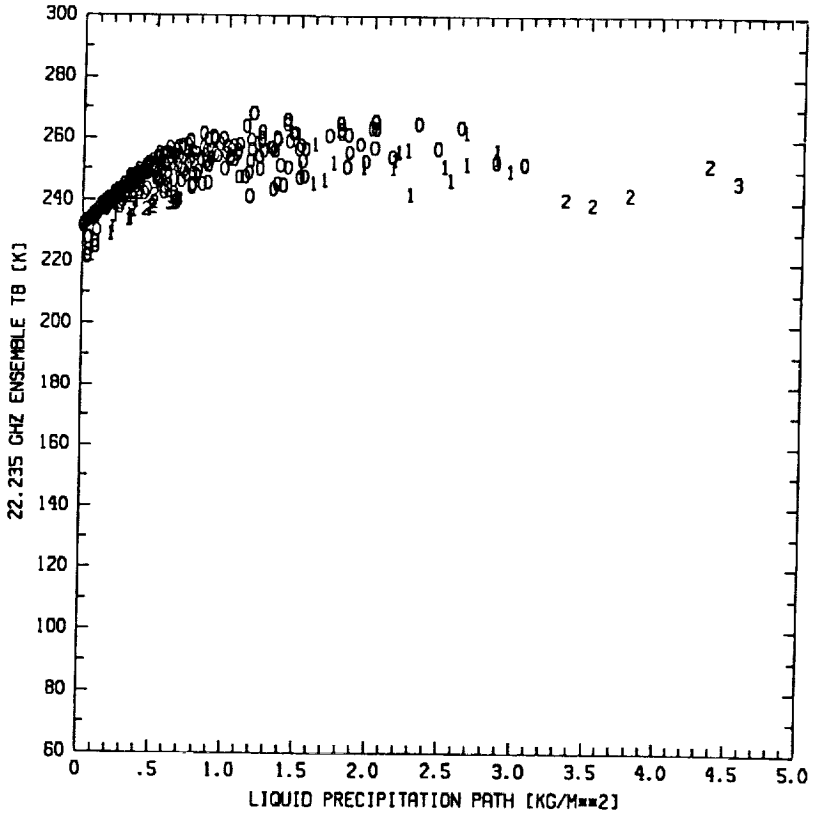

Fig. 8. Plot of cloud ensemble/radiative model brightness temperatures vs. ensemble-average precipitating liquid water paths at (a) 19.35 GHz and (b) 22.235 GHz. Plotted numbers are ensemble-average precipitating ice water paths thresholded at integral values.

(c)

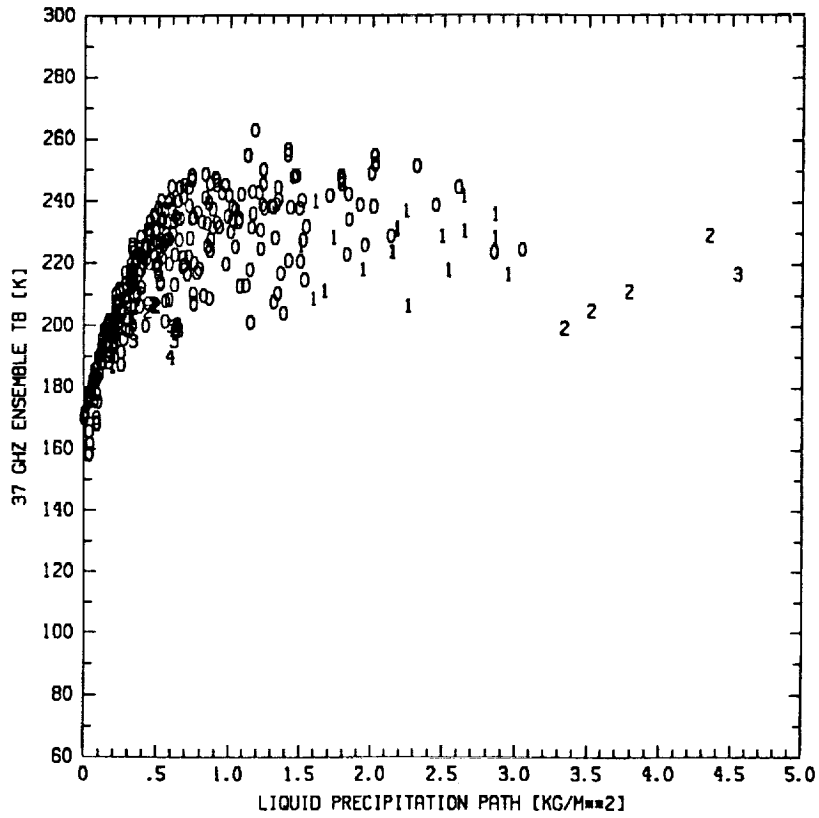

(d)

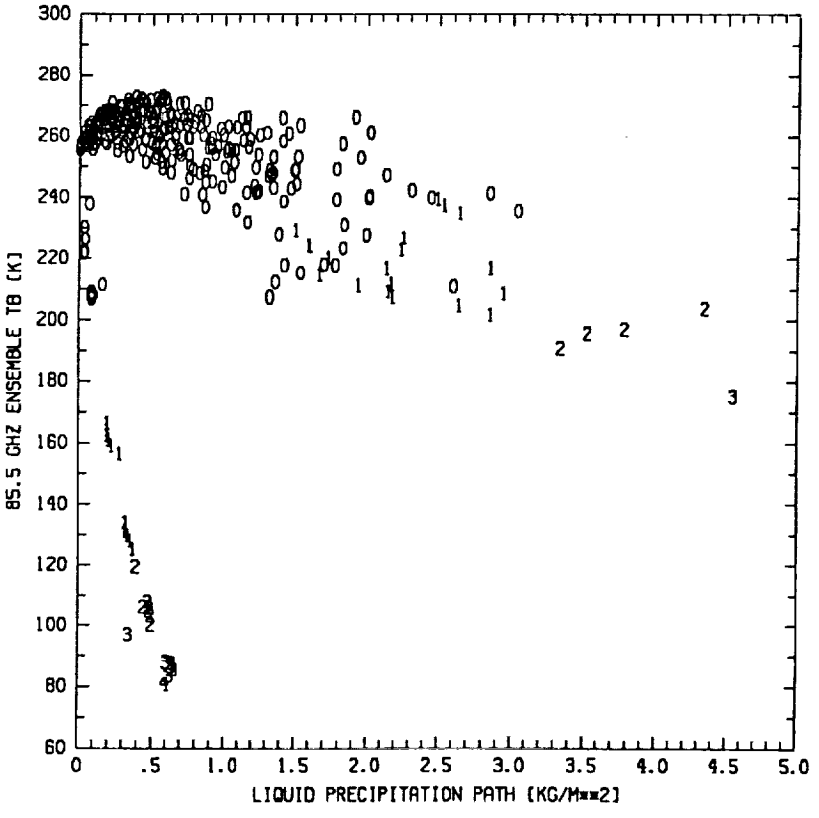

Fig. 8. (cont.) Plot of cloud ensemble/radiative model brightness temperatures vs. ensemble-average precipitating liquid water paths at (c) 37 GHz and (d) 85.5 GHz. Plotted numbers are ensemble-average precipitating ice water paths thresholded at integral values.

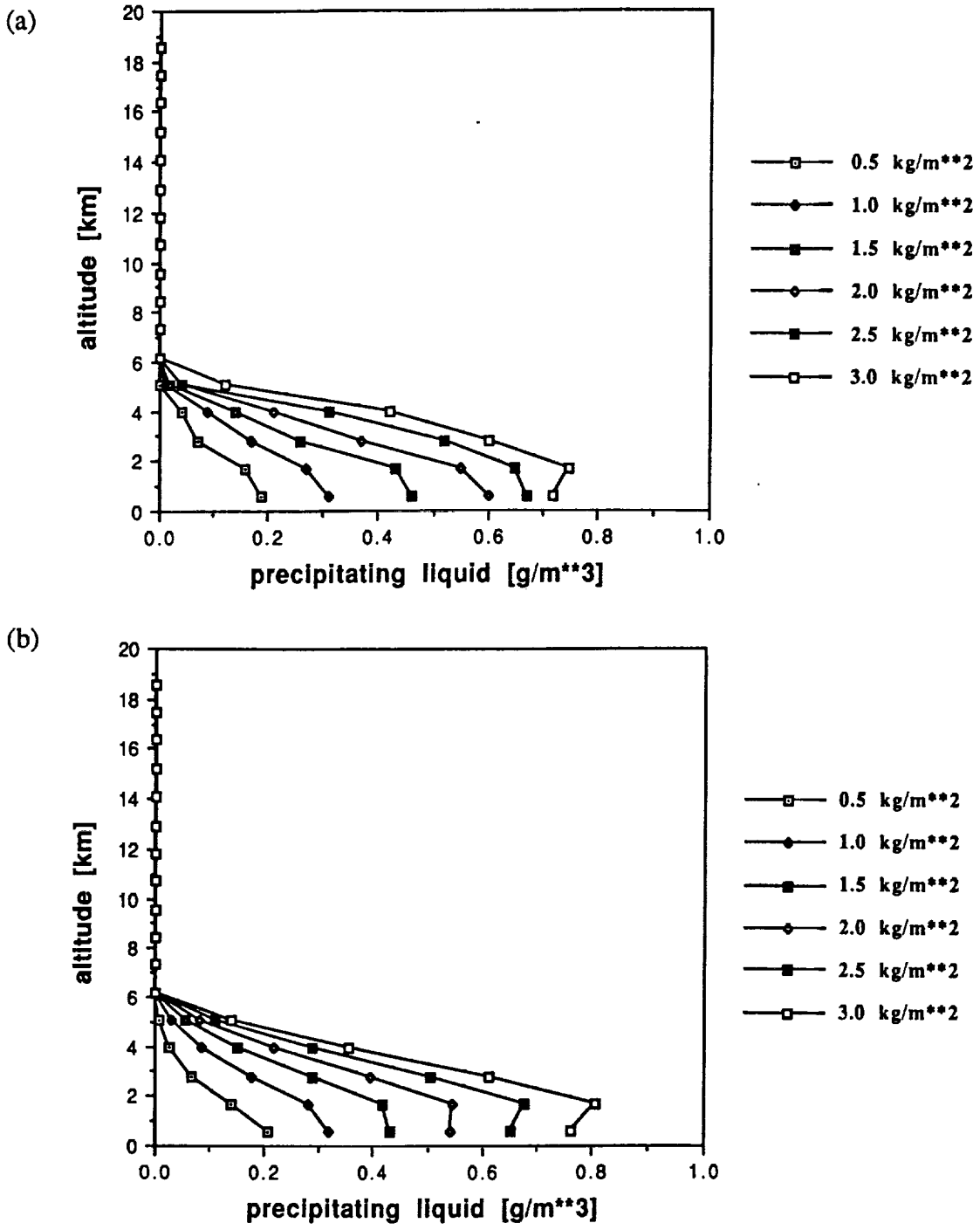

Fig. 9. Mean profiles of precipitating liquid water from (a) the convective cloud ensemble simulations, and (b) the analytical curve fits described in the text. Profiles are shown for precipitating liquid paths of 0.5, 1.0, 1.5, 2.0, 2.5, and 3.0 kg/m^2.

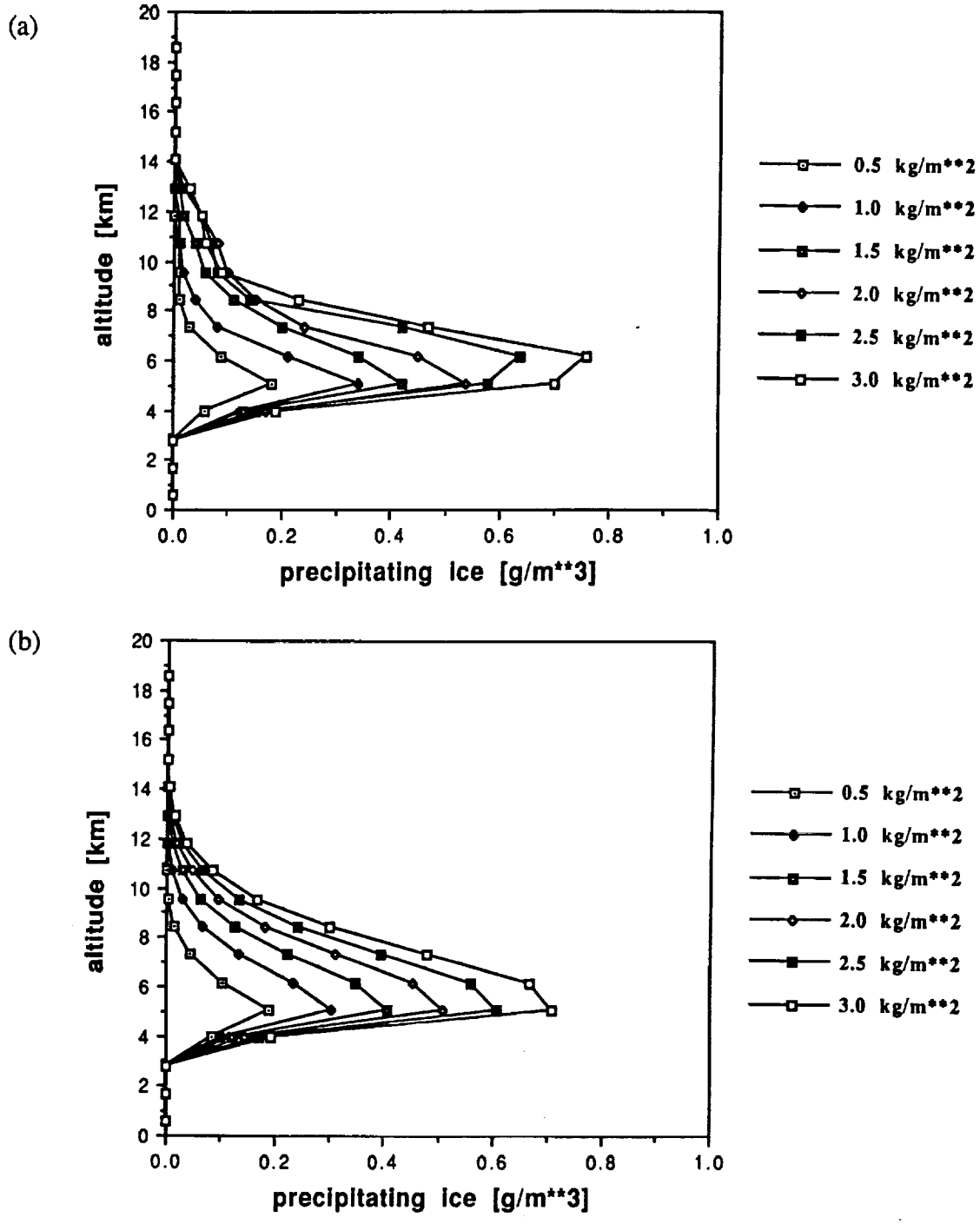

Fig. 10. Mean profiles of precipitating ice from (a) the convective cloud ensemble simulations, and (b) the analytical curve fits described in the text. Profiles are shown for precipitating ice paths of 0.5, 1.0, 1.5, 2.0, 2.5, and 3.0 kg/m^2.

(a)

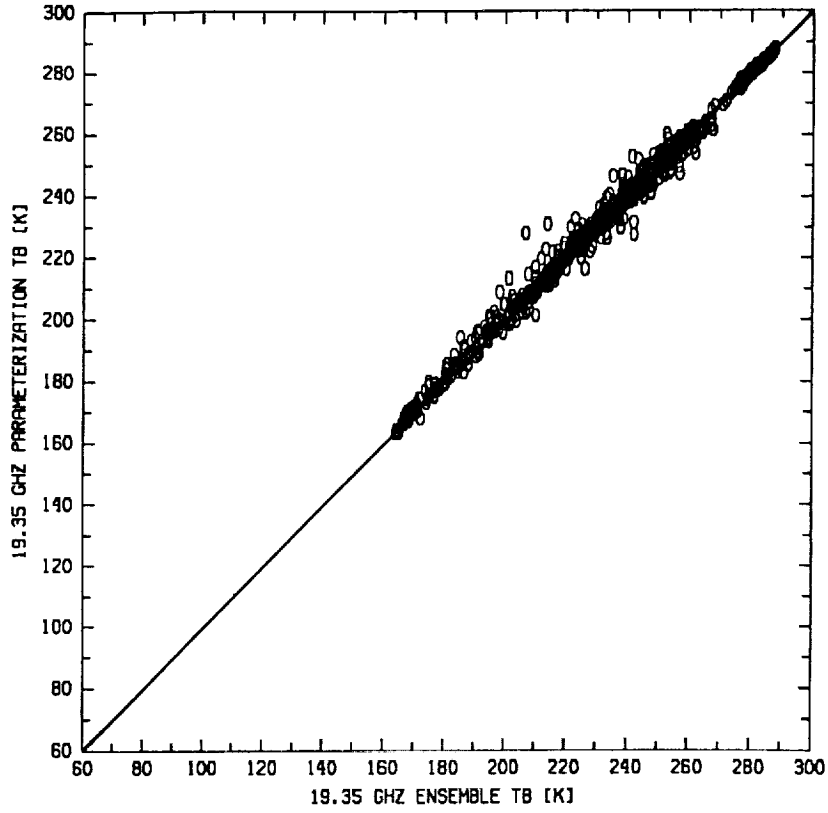

(b)

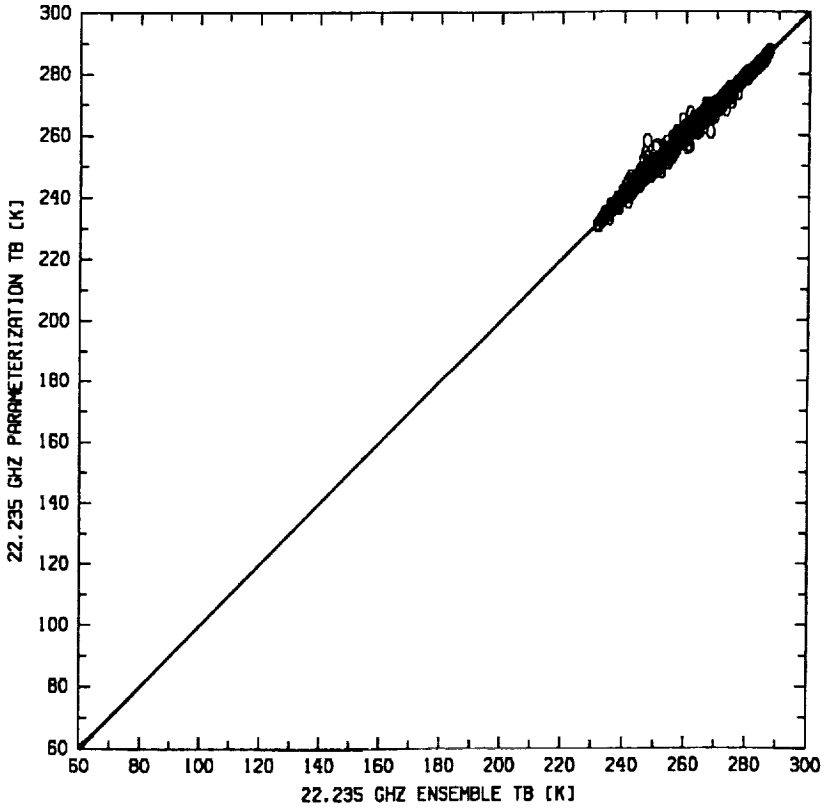

Fig. 11. Plot of parameterized brightness temperatures vs. cloud ensemble/radiative model brightness temperatures at (a) 19.35 GHz and (b) 22.235 GHz. For reference, the solid line in each panel represents a perfect correlation.

(c)

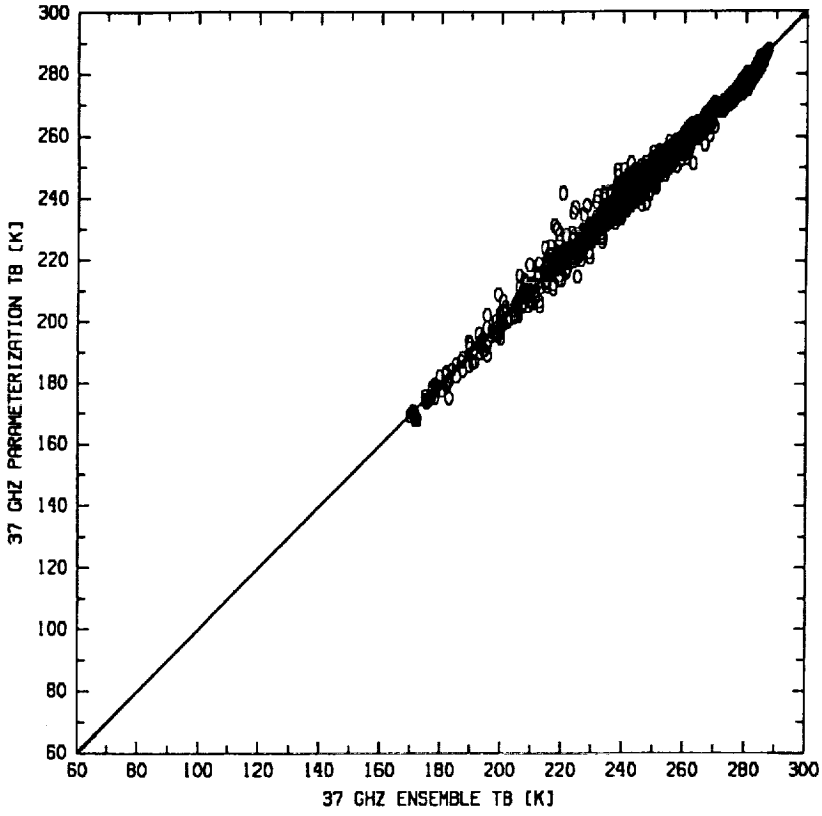

(d)

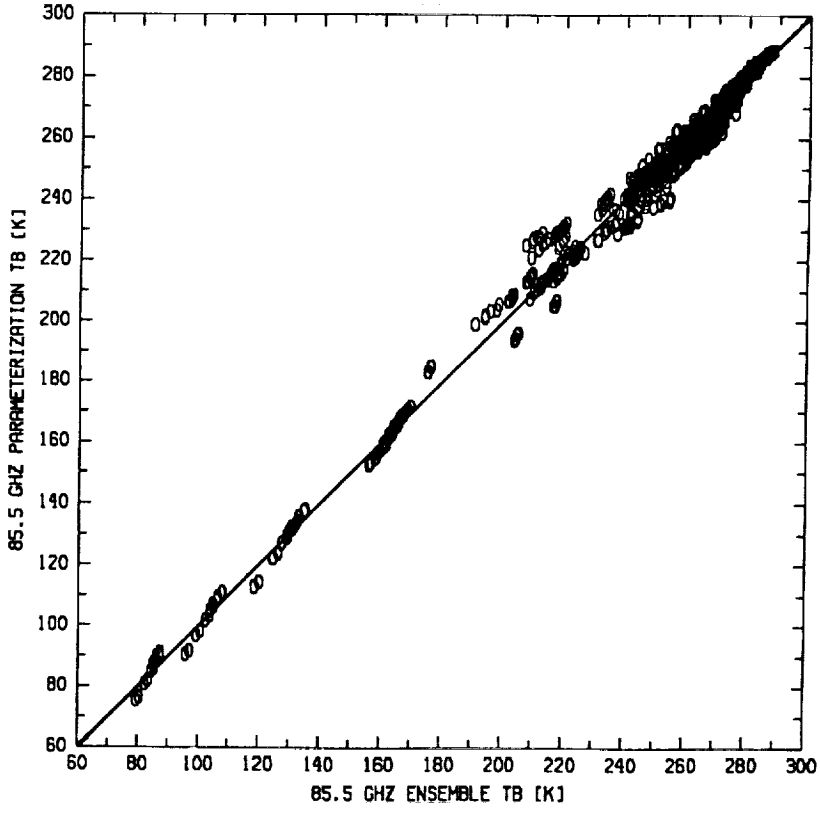

Fig. 11. (cont.) Plot of parameterized brightness temperatures vs. cloud ensemble/radiative model brightness temperatures at (c) 37 GHz and (d) 85.5 GHz. For reference, the solid line in each panel represents a perfect correlation.

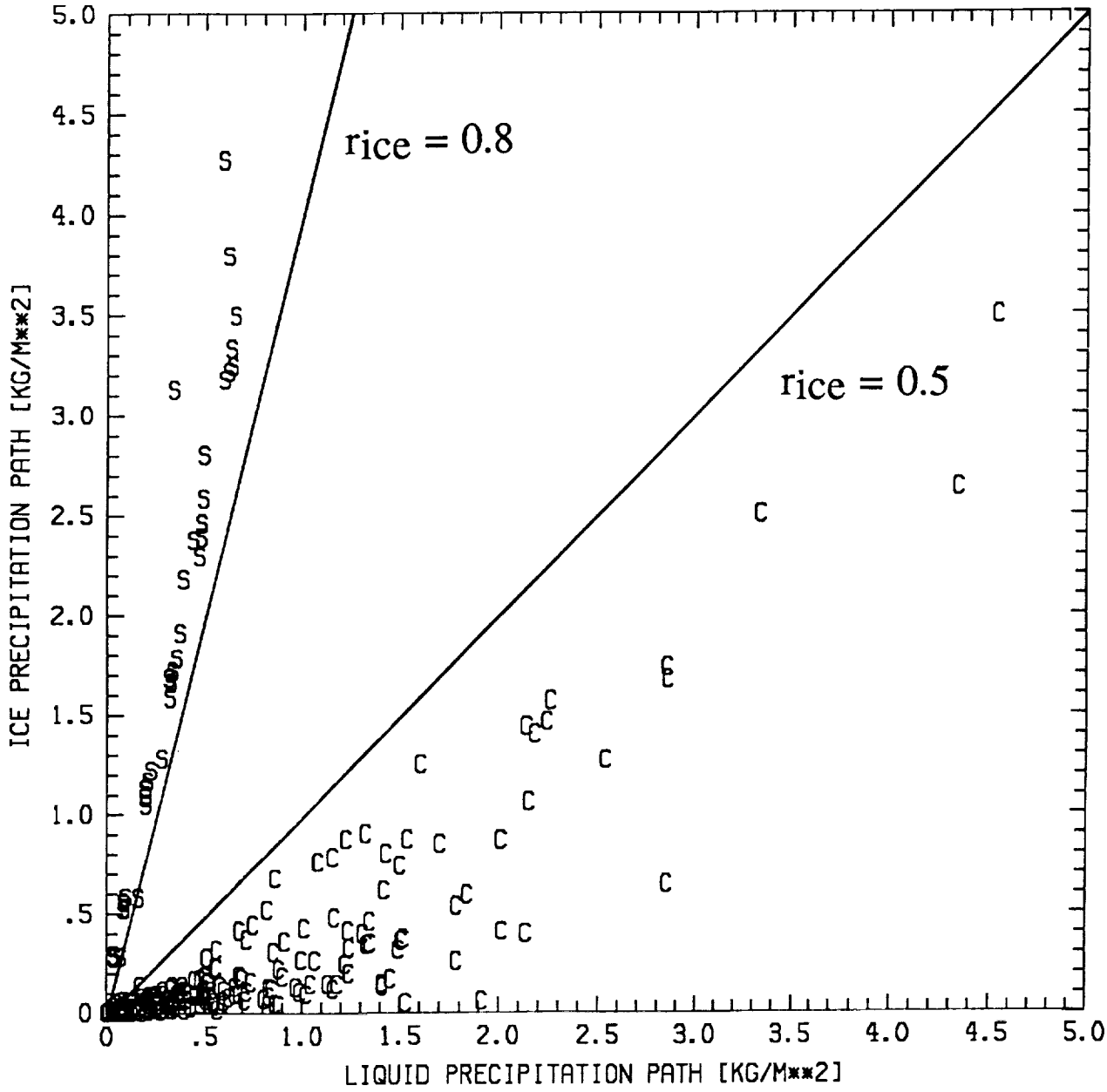

Fig. 12. Scatterplot of ice precipitation path versus liquid precipitation path from both the convective cloud ensemble (C) and stratiform cloud ensemble (S) simulations. Ice to total precipitation path ratios of 0.5 and 0.8 are indicated by solid lines.